Laser Doppler Velocimetry Measurements of Acoustic–Turbulent Flow Interaction Over a Liner

Laser Doppler Velocimetry measurements of Acoustic–Turbulent Flow Interaction over a Liner

Ludovic Ambrosiani[1,2*], Estelle Piot[1†], Fabien Mery[1‡] and Francesco Avallone[2§]
[1]*DMPE, ONERA, Université de Toulouse, 31000, Toulouse, France*
[2]*Politecnico di Torino, Corso Duca degli Abruzzi 24, 10129, Torino, Italy*

The interaction between a grazing turbulent boundary layer at Mach 0.3 and tonal acoustic waves with an amplitude equal to 145 dB over a single-degree-of-freedom acoustic liner is investigated experimentally using Laser Doppler Velocimetry. Streamwise and wall-normal velocity profiles are measured along the liner, and the acoustic-induced velocity component is extracted from time-resolved measurements via a turbulence-rejection technique, allowing the separation of coherent acoustic and turbulent velocity fluctuations within the boundary layer. The influence of the acoustic source position—upstream or downstream of the liner—is examined. Results show that acoustic excitation near liner resonance frequency reduces the near-wall streamwise mean velocity while enhancing velocity fluctuations, producing a localized hump in second-order statistics. The spatial distribution and amplitude of the acoustic-induced velocity above the liner are strongly dependent on source position, and exhibit significant distortions within the near-wall region, revealing a pronounced distortion of the plane wave acoustic field. These measurements provide direct experimental evidence that the turbulent boundary layer modifies the structure of the propagating acoustic wave. These observations highlight that source orientation significantly modulates the transfer of acoustic energy to the turbulent boundary layer, providing new insights into the mechanisms governing acoustic–turbulence interactions over lined surfaces.

I. Nomenclature

c_0	=	Speed of sound in air [$\mathrm{m\,s^{-1}}$]
d	=	Orifice diameter [m]
f_e	=	Forcing frequency of acoustic excitation [Hz]
f_0	=	Resonance frequency [Hz]
h	=	Half-height of the channel [m]
H_c	=	Cavity depth [m]
L	=	Liner streamwise length [m]
L_z	=	Liner spanwise length [m]
LDV	=	Laser Doppler Velocimetry [-]
M_b	=	Bulk Mach number [-]
PSD	=	Power Spectral Density [$\mathrm{m^2\,s^{-2}\,Hz^{-1}}$]
Re_b	=	Bulk Reynolds number [-]
R_f	=	Cavity fillet radius [m]
$s(t)$	=	Reference coherent signal [V]
SDOF	=	Single Degree of Freedom [-]
SPL	=	Sound Pressure Level [dB]
U, V	=	Mean velocity components in x, y [$\mathrm{m\,s^{-1}}$]
U_0	=	Baseline streamwise mean velocity [$\mathrm{m\,s^{-1}}$]
U_b	=	Bulk velocity [$\mathrm{m\,s^{-1}}$]

*PhD student, Multi-physics department for energetics (DMPE) & Department of Mechanical and Aerospace Engineering (DIMEAS), ludovic.ambrosiani@polito.it.
†Research Scientist, Multi-physics department for energetics (DMPE), estelle.piot@onera.fr.
‡Research Scientist, Multi-physics department for energetics (DMPE), fabien.mery@onera.fr.
§Professor, Department of Mechanical and Aerospace Engineering (DIMEAS), francesco.avallone@polito.it.

u_{ac}, v_{ac}	=	Acoustic-induced velocity components in x, y [$\mathrm{m\,s^{-1}}$]
$\tilde{u}_{ac}, \tilde{v}_{ac}$	=	Complex acoustic-induced velocity components in x, y [$\mathrm{m\,s^{-1}}$]
u_{tot}, v_{tot}	=	Instantaneous velocity components in x, y [$\mathrm{m\,s^{-1}}$]
u_{turb}, v_{turb}	=	Turbulent velocity components in x, y [$\mathrm{m\,s^{-1}}$]
u', v'	=	Fluctuating velocity components in x, y [$\mathrm{m\,s^{-1}}$]
Z, θ, χ	=	Normalized acoustic impedance, resistance, reactance [-]
$\tilde{p}_{ac}$	=	Complex acoustic pressure [Pa]
$\delta_{i\in[1,2]}$	=	Neck-length end-correction terms [m]
ν	=	Kinematic viscosity of air [$\mathrm{m^2\,s^{-1}}$]
ρ_0	=	Mean air density [$\mathrm{kg\,m^{-3}}$]
σ	=	Perforated plate porosity [-]
τ	=	Plate thickness [m]
ω	=	Angular frequency [$\mathrm{rad\,s^{-1}}$]

II. Introduction

Acoustic liners are essential components for reducing broadband and tonal noise in turbofan engine ducts [1]. The development of ultra-high bypass ratio engines with larger fan diameters has intensified fan-related noise, including tonal components at the blade-passing frequency (BPF) and broadband noise generated by rotor–stator interaction [2, 3]. To mitigate these sources, a wide variety of liner geometries have been developed and tested over the past decades [4, 5].

Conventional single degree-of-freedom (SDOF) liners consist of a perforated plate backed by a cavity and rigid walls, operating as resonant systems tuned to target frequencies [1]. Their acoustic performance is commonly characterized through an effective acoustic impedance, defined in the frequency domain as

$$Z(\omega) = \frac{\tilde{p}_{ac}(\omega)}{\rho_0 c_0 \tilde{v}_{ac}(\omega)}, \tag{1}$$

where $\widetilde{p}_{ac}(\omega)$ is the Fourier transform of the acoustic pressure, $\widetilde{v}_{ac}(\omega)$ is the Fourier transform of the acoustic particle velocity normal to the liner surface, ρ_0 is the mean density, and c_0 the speed of sound. The impedance is a complex number, where $\theta = \mathrm{Re}(Z)$ and $\chi = \mathrm{Im}(Z)$ denote the resistance and reactance, respectively.

Although acoustic impedance is often regarded as an intrinsic property of the liner surface, numerous studies have shown that its eduction is highly sensitive to the experimental or numerical methodology employed [6]. In particular, the presence of a grazing flow significantly alters the acoustic response of liners, with strong dependencies reported on boundary-layer properties such as turbulent boundary layer thickness [7]. These observations have motivated the development of impedance models and eduction procedures that explicitly account for the grazing-flow boundary layer and the local decay of sound pressure level along the liner [8–11]. In addition, discrepancies reported between upstream- and downstream-propagating acoustic waves [12] continue to challenge our understanding of liner-flow-acoustic interactions in the near-wall region.

From a physical perspective, the interaction between a turbulent boundary layer and a liner subjected to grazing acoustic excitation is inherently coupled. The grazing flow modifies the acoustic field through refraction, dissipation, and shear-layer effects, while the acoustic forcing can in turn alter the near-wall aerodynamic field. Understanding this bidirectional coupling therefore requires detailed measurements of the local flow dynamics in the immediate vicinity of the liner surface.

Early numerical efforts addressed this problem by resolving sound interaction with laminar and turbulent boundary layers at the scale of a single orifice [13]. While these simulations provided valuable insight into local flow-acoustic mechanisms, they were limited to single-resonator configurations and did not account for the streamwise development of the boundary layer over multi-cavity liners. Experimentally, Léon et al. [14] investigated the near-wall aerodynamic response of a liner grazed by a turbulent flow using high-magnification particle image velocimetry. Their results highlighted the influence of acoustic excitation, flow velocity, and resonance conditions on the mean velocity field and demonstrated that simple rough-wall analogies fail to capture the observed behavior. However, the investigation was limited to a single acoustic source position and moderate Mach numbers because of experimental constraints, and it did not provide detailed temporal information on the flow response.

Complementary insight has also been provided by high-fidelity numerical simulations. Recently, pore-resolved compressible simulations by Shahzad et al. [15] examined turbulent flow over a multi-cavity acoustic liner in the

absence of acoustic forcing. Their results revealed that the liner induces a restructuring of near-wall turbulent structures, exhibiting similarities with flows over porous surfaces. Building on these findings, Paduano et al. [16] performed high-fidelity lattice-Boltzmann very-large-eddy simulations of a turbulent boundary layer interacting with a multi-cavity liner subjected to grazing acoustic waves [17]. Their study demonstrated that the streamwise development of the boundary layer leads to significant spatial variations of the acoustic impedance along the liner. In particular, the turbulent boundary layer is progressively displaced away from the liner surface downstream of the orifices, modifying the shear-layer dynamics and the acoustic-induced mass flow within the cavities. These results highlight the critical role played by boundary-layer development in shaping the acoustic response of liners under grazing flow conditions [18].

Experimental investigations capable of resolving the local aerodynamic and acoustic response of a turbulent boundary layer interacting with a liner under grazing acoustic excitation remain scarce. Direct measurements of mean flow modifications, turbulence intensities, and the spectral redistribution of velocity fluctuations above the liner surface are still limited, especially when different acoustic source positions are considered. Furthermore, time-resolved measurements capable of separating turbulent and acoustic velocity fluctuations in the near-wall region remain largely absent from the literature. Such measurements are experimentally challenging, as they require sufficiently high temporal resolution to capture turbulent fluctuations while simultaneously resolving the coherent acoustic contribution in the near-wall region. As a result, the local structure of the acoustic field within the boundary layer, and its modification through interaction with turbulence, remains poorly documented experimentally.

The objective of the present study is to experimentally characterize both the aerodynamic response of the turbulent boundary layer and the local acoustic field associated with a grazing acoustic wave over a flush-mounted multi-orifice liner. Laser Doppler Velocimetry (LDV) is employed to provide non-intrusive, time-resolved measurements of the mean velocity field, second-order statistics, and power spectral densities of the streamwise and wall-normal velocity components. In addition, the time-resolved measurements enable the extraction of the acoustic-induced velocity field, allowing the coherent acoustic velocity components to be quantified within the turbulent boundary layer. The influence of the acoustic source position is investigated by introducing the grazing acoustic wave either upstream or downstream of the lined section. This approach provides direct experimental access to the spatial evolution of the acoustic-induced velocity field and enables the assessment of how the acoustic wave itself is modified through its interaction with the turbulent boundary layer.

The remainder of the paper is organized as follows. Section III describes the experimental facility, the acoustic liner configuration, and the LDV measurement methodology. Section IV presents the acoustic characterization of the liner and highlights the differences in sound pressure level distribution along the liner for upstream and downstream acoustic excitation. Section V examines the aerodynamic response of the turbulent boundary layer through the analysis of mean velocity profiles and second-order statistics. Section VI investigates the spectral redistribution of velocity fluctuations under acoustic forcing. Section VII focuses on the acoustic-induced velocity field extracted from the LDV measurements and discusses the modification of the acoustic wave as it interacts with the turbulent boundary layer. Finally, Section VIII summarizes the main findings and outlines perspectives for future work.

III. Experimental setup

A. Aero Thermo Acoustic Duct

The measurements were carried out at ONERA Toulouse in the B2A aero-thermo-acoustic facility, illustrated in Fig. 1. This facility is specifically designed to investigate the aerodynamic and acoustic response of liners subjected to turbulent grazing flow and to acoustic excitation generated either upstream or downstream of the liner.

The B2A is a rigid square duct of cross-section 50×50 mm^2, acting as a waveguide with a plane-wave cutoff frequency of approximately 3450 Hz in the absence of flow. The test section accommodates liner samples up to $L = 150$ mm in streamwise length and 50 mm in spanwise width, flush-mounted in the lower wall. Optical access is provided on both sides of the test section with silica windows.

A fully developed turbulent flow enters the test section with a centerline turbulence intensity of approximately 5%. The static temperature is controlled at $T_0 = 20°$C, and the mass flow rate is regulated at 300 g s^{-1}, yielding a bulk velocity of $U_b \approx 100$ m s^{-1}. With the ambient speed of sound $c_0 = 343$ m s^{-1}, the bulk Mach number is

$$M_b = \frac{U_b}{c_0} \approx 0.3. \tag{2}$$

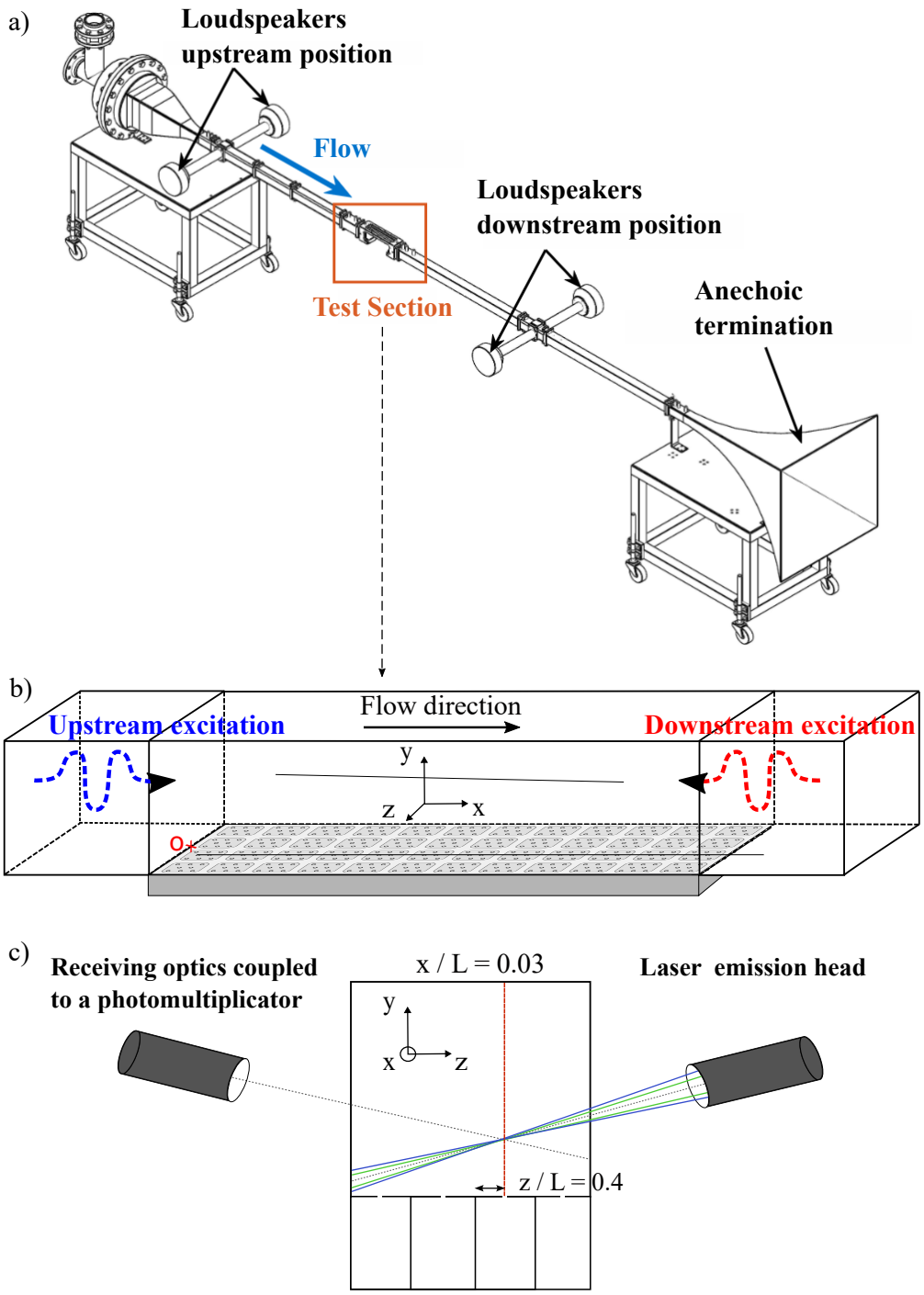

Fig. 1 Schematic of a) the B2A duct, b) test section, flow and acoustic waves, and c) LDV setup in a plane over orifices.

Using the half-height $h = 25\text{mm}$ and the kinematic viscosity $\nu = 1.51 \times 10^{-5}\ \text{m}^2\,\text{s}^{-1}$, the bulk Reynolds number is

$$\text{Re}_b = \frac{2U_b h}{\nu} \approx 3.3 \times 10^5. \tag{3}$$

B. Acoustic Excitation and Pressure Measurements

Acoustic excitation is provided by two loudspeakers, which can be mounted symmetrically 1.3 m upstream and downstream of the test section. They generate plane acoustic waves and allow tonal excitation with sound pressure levels (SPL) up to 150 dB.

A quasi-anechoic termination at the duct outlet provides an acoustic reflection coefficient below 0.2 above 500 Hz. The inlet reflection coefficient is measured and included in the impedance eduction procedure.

The source amplitude is adjusted to obtain a prescribed incident acoustic pressure level. Six microphone locations are distributed along the upper wall, enabling acoustic pressure measurements either upstream of the liner leading edge or downstream of the liner trailing edge. Two flush-mounted GRAS microphone probes are used (probe diameter of 1.2 mm) to perform a wave decomposition and to measure the SPL at the wall opposite the liner via a wave-sorting procedure [19].

The upper wall facing the liner is equipped with 16 microphone locations. Wall-pressure measurements are performed using a single microphone probe successively positioned at each location. This procedure avoids phase mismatch between pressure measurements. A short-time Fourier transform is then applied to each pressure signal to extract the spectral content, from which the SPL is computed using the amplitude of the acoustic pressure fluctuations.

C. Description of the Acoustic Liner Geometry

The liner is an SDOF consisting of a perforated plate over a layer of square cavities, as illustrated in Fig. 2. The liner geometry is shared across several institutions and has already been investigated in multiple studies [16, 20, 21]. The geometrical parameters are summarized in Table 1 and are described below.

The sample contains 12 cavities in the streamwise direction and 4 in the spanwise direction. Each cavity is a rounded square of mean width 9.95 mm, fillet radius $\approx$ 2 mm, and depth $H_c = 38.1 \pm 0.1$ mm. The liner sample has been machine-drilled in a single block of aluminum to better control the dimensions.

Table 1 Geometrical and acoustic parameters of the SDOF liner.

Parameter	Symbol	Value
Liner streamwise length	L	150 mm
Liner spanwise length	L_z	50 mm
Cavity mean width	D	9.95 mm
Cavity fillet radius	R_f	$\approx$ 2 mm
Number of cavities (streamwise)	N_x	12
Number of cavities (spanwise)	N_z	4
Cavity depth	H_c	38.1 ± 0.1 mm
Face sheet thickness	l^*	0.63 ± 0.01 mm
Orifice diameter	d	0.99 ± 0.01 mm
Number of holes per cavity	N_h	8
Global porosity	σ	3.95%
Minimum space between holes	l_0	3.31 mm
Resonance frequency without flow	f_0	$\approx$ 1450 Hz

The perforated plate has thickness $l^* = 0.63 \pm 0.01$ mm and contains circular orifices of diameter $d = 0.99 \pm 0.01$ mm arranged in groups of eight per cavity. The global porosity, defined as the ratio of the total perforation area to the total liner surface area, is

$$\sigma = \frac{N_{tot}\,\pi d^2}{4 L L_z}. \tag{4}$$

with $N_{tot} = N_x N_z N_h$ the total number of holes. L and L_z denote the streamwise and spanwise dimensions of the liner surface.

The resonance frequency $\omega_0 = 2\pi f_0$ of an equivalent isolated resonator with a single orifice can be estimated following the model of Rienstra and Singh [22]:

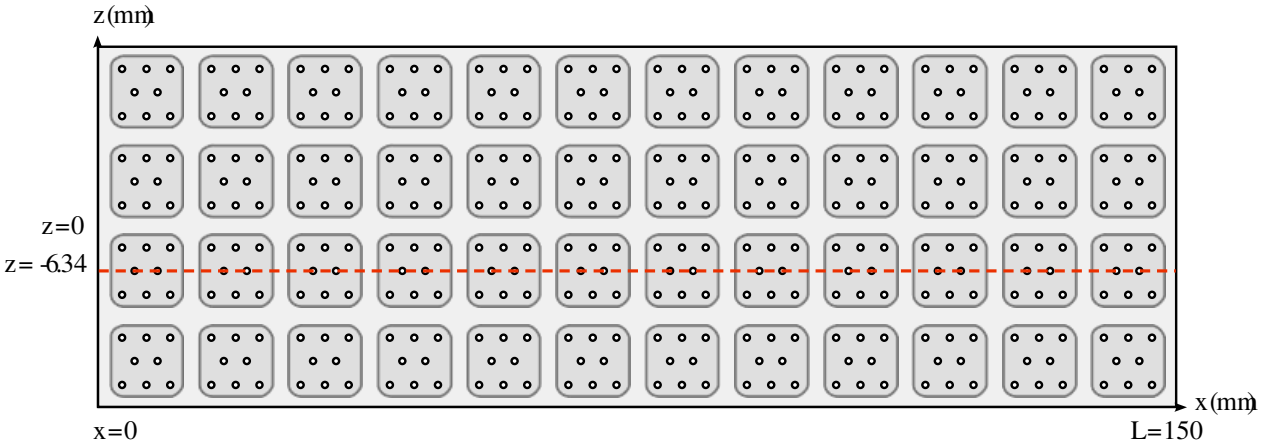

Fig. 2 Top view of the SDOF liner sample showing cavity layout and LDV measurement plane in dashed red line.

$$\kappa_0 \tan(\kappa_0) = \frac{H_c S_n}{l S_h}, \quad \text{with} \quad \kappa_0 = \frac{\omega_0 H_c}{c_0}, \tag{5}$$

where $l = l^* + \delta_1 + \delta_2$ is the effective orifice neck length, including the inner and outer end corrections. These corrections account for the air inertia on both sides of the face sheet and are approximated by $\delta_i \approx 0.85(S_n/\pi)^{1/2}(1 - 1.25\xi_i)$, with $\xi_1 = d/D$ and $\xi_2 = 0$. The terms S_n and S_h refer to the cross-sectional areas of the neck and the cavity, respectively. Solving the resonance condition yields a fundamental resonance frequency of approximately $f_0 \approx 1450$ Hz in the absence of flow.

D. LDV System, Optical Configuration, and Seeding

A two-component Laser Doppler Velocimetry system is used to measure the streamwise and wall-normal velocity components (u, v) above the liner. The optical arrangement uses a 1 W SpectraPhysics argon–ion laser emitting at 488.5 and 514.5 nm. Each laser beam is split into two beams using a prism, with one beam in each pair frequency-shifted by 40 MHz using a Bragg cell. Two independent beam pairs are formed this way and focused with a Dantec transmitter with a 240 mm focal-length lens with a beam spacing of 30 mm. The resulting ellipsoidal measurement volume is approximately 0.08 mm in the transverse directions and 0.7 mm along the beam axis. The two measurement directions are tilted by approximately 45° with respect to the horizontal and vertical axes to balance the uncertainty on each component. The rotation matrix used to reconstruct (u, v) is determined from a calibration performed with a theodolite to characterize the angle of each laser beam. From this calibration data, the fringe spacing is computed for each component and gives 2.2344 ± 0.0064 μm for the green beam and 2.1544 ± 0.0057 μm for the blue beam.

The LDV probe is mounted on a three-axis traverse and operated in forward-scatter configuration to increase signal-to-noise ratio and data rate. Measurements are taken along wall-normal profiles at a fixed spanwise location, $z = -6.34$ mm, relative to the liner centerline, above a row of cavities, as indicated by the red dashed line in Fig. 2. Each profile contains 60 exponentially spaced points, providing increased resolution near the liner surface.

The flow is seeded with fumed silica particles R972 of primary diameter ~ 20 nm, forming aggregates up to 0.2 μm. Their relaxation time is much smaller than the acoustic period at 1500 Hz, ensuring adequate velocity tracking.

At each measurement location, the LDV records the Doppler burst in a coincidence mode between the two components with a validation rate typically around 97%. The Doppler frequency f_b of each burst is saved for both components. Typical mean data rates peak at 20–30 kHz in the middle of the test section and decrease to approximately 10 kHz near the liner surface. For each location, $N = 250{,}000$ Doppler bursts are recorded, resulting in measurement durations ranging from 8 to 20 seconds. The exported data include the burst arrival time, particle transit time, burst frequency of both components, and the analog reference signal sent to the loudspeakers.

The two velocity components (u, v) are obtained by multiplying the measured Doppler frequencies by the corresponding fringe spacings and then applying the calibration rotation matrix.

E. Velocity Decomposition and Processing

The instantaneous velocity components measured are decomposed as

$$u_{tot}(t) = U + u_{turb}(t) + u_{ac}(t), \qquad v_{tot}(t) = V + v_{turb}(t) + v_{ac}(t), \tag{6}$$

where U,V denote the mean velocities, u_{turb},v_{turb} the turbulent fluctuations and u_{ac},v_{ac} the coherent acoustic-induced velocities. In contrast to the mean quantities, we define the total fluctuating velocities as

$$u'(t) = u_{tot}(t) - U, \qquad v'(t) = v_{tot}(t) - V, \tag{7}$$

which represent the cumulative unsteady contributions arising from turbulence and acoustic forcing.

We denote by u_{rms} and v_{rms} the root-mean-square values of the fluctuating velocities:

$$u_{\mathrm{rms}} = \sqrt{\frac{1}{N_t}\sum_{i=1}^{N_t} u'(t_i)^2}, \qquad v_{\mathrm{rms}} = \sqrt{\frac{1}{N_t}\sum_{i=1}^{N_t} v'(t_i)^2}, \tag{8}$$

with N_t the number of samples in the time-domain signal.

The irregularly sampled LDV data are interpolated onto a uniform time base using the inverse of the mean interarrival time between bursts, providing an effective sampling frequency of $f_s \approx$ 10–20 kHz (depending on the wall-normal position). This interpolation enables computation of auto- and cross-spectral densities using the Welch algorithm. The calculation utilized a 50% overlap, a Hanning window, and a window size of $f_s/2$ samples. The resulting spectra provide insight into the distribution of fluctuation energy across frequencies.

Post-processing and statistical evaluation are performed using a dedicated Python analysis toolchain (based on the in-house ONERA software ASSA [23]) applied independently to u and v velocity components.

The tonal electric signal sent to the loudspeaker is saved at each arrival time of the burst resulting in a synchronized reference acoustic signal s(t) which is a pure tone at the frequency f_e.

The acoustic-induced velocity components, $\tilde{u}_{ac}(f_e)$ and $\tilde{v}_{ac}(f_e)$, are extracted at the excitation frequency f_e using a tonal bias-correction procedure based on coherent processing with the acoustic reference signal s(t), following Minotti et al. [24]. The complex cross-spectrum between the velocity signal and the reference (here the acoustic source signal) is computed at f_e and normalized by the auto-spectrum of the reference to isolate the velocity contribution coherent with the acoustic excitation. Parseval's theorem is then used to determine the amplitude of the acoustic-induced fluctuations $|\tilde{u}_{ac}|$ and $|\tilde{v}_{ac}|$. The phases ϕ_u and ϕ_v extracted from the cross-spectral analysis correspond to the phase of the coherent acoustic velocity component relative to the acoustic reference signal. They therefore represent the local propagation and interaction effects of the acoustic wave with the mean flow and the liner surface. An estimate of the uncertainty in both the amplitude and phase of the acoustic-induced velocity is obtained using a bootstrap method, following Léon et al. [25].

The remaining incoherent part of the spectrum is attributed to broadband turbulence and measurement noise. This approach enables a clear separation between the coherent acoustic component and the turbulent background when the former is buried within the latter [14]. This method is commonly used in LDV-based liner impedance eduction studies [26].

F. Measurement Uncertainty Estimation

As in most laser-based velocimetry techniques, the estimation of measurement uncertainty in LDV is not straightforward. In the present work, the uncertainty analysis considers the uncertainty on the burst analyzer frequency response, estimated using a frequency generator, and the uncertainty on the optical setup, i.e., the uncertainty on the fringe spacing.

Uncertainties in the optical setup were quantified using a Monte Carlo approach. Based on the available measurements and parameters from the calibration, synthetic sets were generated by introducing random perturbations in the laser wavelengths, beam angles and temperature for each draw. These perturbed values were then used to recalculate the corresponding calibration parameters. After 10,000 iterations, the distributions obtained for each of the parameters were used to estimate the standard uncertainties associated with the fringe spacing.

The resulting relative uncertainties, of the order of 0.1–0.3%, directly affect both mean and r.m.s. velocities and remain fully correlated across the entire dataset. Overall, the bounds of the 95% confidence intervals obtained for the projected mean and r.m.s. velocities remain modest. Even in the most unfavorable conditions, where both error sources contribute significantly, the uncertainty on the mean velocity typically remains below ±0.3% of its value, while the relative uncertainty on the r.m.s. level remains below ±0.35%.

These uncertainty levels are deemed adequate for the present study, as the fluctuations of interest are much larger than the estimated measurement errors.

It should nevertheless be stressed that, when comparing the LDV measurements with numerical simulations, additional sources of uncertainty must be considered. Beyond the fringe spacing and frequency response uncertainties discussed above, the LDV technique inherently introduces spatial averaging due to the measurement volume size ($0.08 \times 0.08 \times 0.7$ mm^3), and the precise positioning of the measurement volume relative to the liner is not perfectly known with an estimated positioning precision of the order of 10 μm. These factors contribute to the overall error budget and should be considered in any detailed comparison with simulations.

IV. Acoustic characterization and source-dependent SPL distribution along the liner

Before analyzing the velocity measurements, it is necessary to characterize the acoustic pressure field established in the duct for the two source configurations considered in this study. Because the acoustic source can be positioned either upstream or downstream of the lined section, the resulting sound pressure level distribution along the liner is not identical in the two cases. These differences in acoustic forcing must be quantified in order to properly interpret the LDV measurements and assess how the turbulent boundary layer responds to the imposed acoustic field. The present section therefore provides a characterization of the acoustic pressure distribution along the liner for both source locations.

The acoustic response of the SDOF liner under turbulent grazing flow was characterized experimentally using wall-mounted microphone measurements. The results obtained under the present test conditions are shown in Fig. 3.

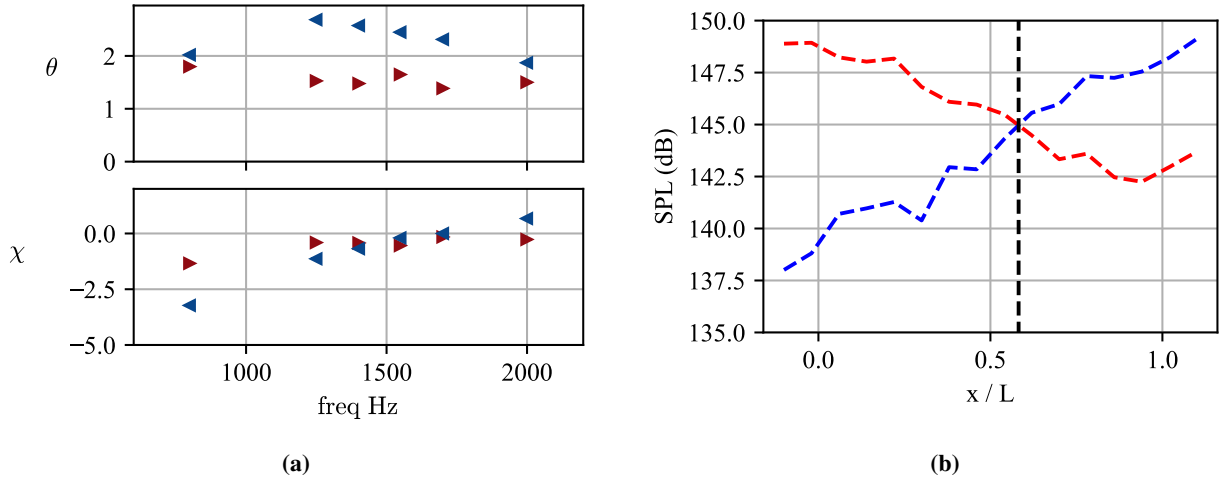

Fig. 3 Acoustic characterization of the liner: (a) impedance and (b) SPL distribution along the liner for both source configurations (upstream in red and downstream in blue).

The impedance of the liner is educed in the frequency domain using an indirect method where two-dimensional linearized Euler equations are solved with a discontinuous Galerkin solver, incorporating a measured shear-flow profile [27]. Results are presented in Fig. 3a. It can be observed that for the case of the downstream acoustic source, the resistance increases compared to the upstream source case, similarly to what was observed in the seminal work of Renou and Aurégan [12]. These discrepancies confirm that the present liner, flow, and SPL conditions are relevant for investigating source-dependent liner behavior.

Second, the total SPL at the wall opposite to the liner is shown in Fig. 3b for a pure-tone excitation at 1500 Hz, close to the resonance frequency. At the beginning of the liner, the incident SPL is set to 145 dB for both the upstream and downstream source configurations, resulting in a total SPL around 149 dB for both configurations as observed on Fig. 3b. A first observation is that the SPL does not decrease symmetrically along the liner for the two source positions in the presence of flow. The SPL decreases much more strongly in the downstream-source configuration. The decay is similar to that observed by Paduano et al. [16]. A particular point of interest is the streamwise location where the total SPL curves cross, meaning an equivalent total SPL of 145 dB at that location for the two configurations. We denote this specific location by x_{eq}, with $x_{eq} \approx 87$mm (located between the 7th and 8th cavities shown in Fig. 2).

For the rest of the study, the acoustic forcing frequency is set to match the configurations observed on Fig. 3b.

Therefore, acoustic excitation is set at $f_e = 1500$ Hz, close to the resonance frequency f_0, with an incident SPL of 145 dB at the entry of the lined section, resulting in a total SPL of 149 dB.

V. Aerodynamic velocity field

This section presents the aerodynamic velocity fields obtained from LDV measurements under both unforced and acoustically forced conditions. Measurements were performed for a bulk Mach number of 0.3 at three streamwise locations along the plate ($x/L = 0.01$, 0.58, and 0.99) to characterize the development of the boundary layer. In addition to the baseline case without acoustic, acoustic forcing at 1500 Hz and 145 dB was applied using upstream and downstream sources to investigate its influence on the velocity field. The experimental test matrix is summarized in Table 2. All velocity profiles are normalized by the centerline velocity U_0, and the wall-normal coordinate is normalized by the channel half-height h.

Table 2 Summary of the LDV experimental test matrix.

Mach	Acoustic source	Forcing frequency	incident SPL	Measurement locations
0.3	–	–	–	$x/L = [0.01, 0.58, 0.99]$
0.3	Upstream	1500 Hz	145 dB	$x/L = [0.01, 0.58, 0.99]$
0.3	Downstream	1500 Hz	145 dB	$x/L = [0.01, 0.58, 0.99]$

A. Aerodynamic response of the liner without acoustic forcing : Baseline case

Fig. 4 presents the streamwise evolution of the grazing turbulent flow over the liner. From left to right, the figure shows the normalized mean velocity U/U_0 followed by the variance of the fluctuating velocity u^2_{rms}/U_0^2 and v^2_{rms}/U_0^2 at three representative streamwise locations ($x/L \approx 0.01$, $x_{eq}/L \approx 0.58$, and $x/L \approx 0.99$).

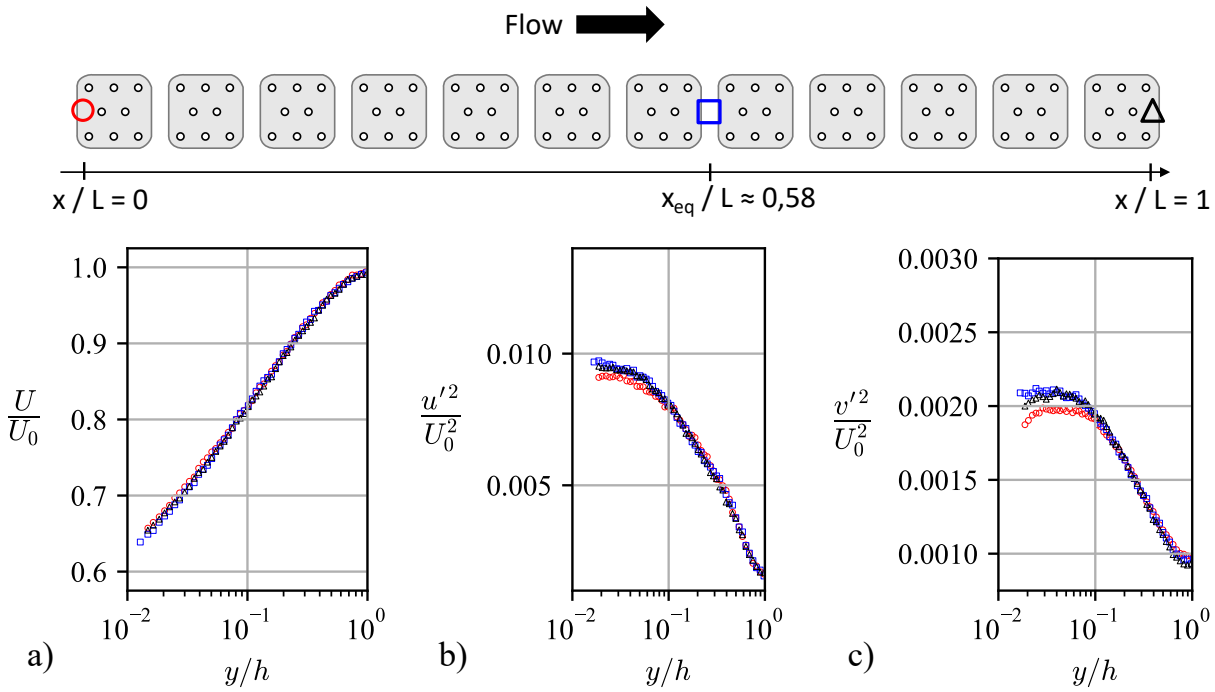

Fig. 4 Mean velocity and fluctuation variances along the liner without acoustic forcing at three streamwise locations represented with colored marker on the scheme.

At the liner leading edge ($x/L = 0.01$), the mean velocity profile already exhibits the signature of an established wall-bounded turbulent flow, with a strong near-wall velocity deficit and a monotonic recovery toward the duct-core

velocity. Downstream, the profile shape changes only moderately, indicating that the liner does not strongly alter the bulk mean flow within the wall-normal range accessible to the LDV measurements. A similar absence of noticeable modification was reported experimentally by Léon et al. [14] in the same duct configuration.

The variance statistics exhibit a stronger streamwise evolution than the mean velocity. The streamwise velocity fluctuations u_{rms}^2/U_0^2 reach their highest values close to the wall. As the flow develops along the liner, both the magnitude and distribution of u_{rms}^2 evolve before approaching a relatively stable profile shape near x_{eq}/L.

The wall-normal fluctuations v_{rms}^2/U_0^2 are consistently smaller than the streamwise component, reflecting the anisotropic character of wall-bounded turbulence. Similar to the streamwise fluctuations, the largest values occur in the near-wall region and decrease toward the outer flow. The streamwise evolution of v_{rms}^2 is more pronounced, suggesting that the primary aerodynamic response of the turbulent grazing flow to the liner is reflected in stronger modifications of the wall-normal turbulent motions, possibly associated with wall-normal transport induced by the perforated surface.

This behavior observed for both components suggests that the liner modifies the near-wall turbulence and promotes the emergence of an outer-layer peak consistent with previous observations of zero-pressure-gradient turbulent boundary layers over porous or perforated surfaces, where wall-normal transport promotes the formation of secondary motions [28].

The strongest variations of fluctuating quantities occur between the leading edge and the intermediate location $x_{eq}/L \approx 0.58$. Downstream of this position, the profiles evolve more weakly, indicating that the turbulent grazing boundary layer progressively adapts to the liner surface. The precise streamwise location at which the turbulent boundary liner adapted to the perforated surface is unknown as it could happen anywhere before the measured location. This idea is consistent with findings on turbulent flow over rough surfaces, where outer-layer features stabilize further downstream [29].

Although the present LDV measurements do not extend sufficiently close to the wall to capture the inner peak of the turbulence intensity commonly observed in the literature [15, 16, 28, 30], the observed enhancement of velocity fluctuations in the accessible region indicates a redistribution of turbulent activity within the boundary layer rather than a uniform amplification across the entire profile.

These results provide a reference baseline and indicate that, within the measurement range considered here, the liner geometry alone does not significantly modify the mean flow. In comparison, the second-order statistics do are affected by the presence of the liner. To better extract the effect of a grazing acoustic wave on the turbulent boundary layer, the results of the next sections will be consistently compared to this baseline case.

B. Effect of grazing acoustic wave on the mean flow

This section examines the modification of the mean flow induced by grazing acoustic excitation over the liner. The objective is to identify the interaction between the acoustic field and the turbulent boundary layer and to assess the influence of the acoustic source position on the mean streamwise velocity evolution along the liner. In all figures, the upstream acoustic source configuration is shown in red, the downstream configuration in blue, and the baseline case without acoustic forcing in black.

The mean streamwise velocity profiles obtained under grazing acoustic excitation are shown in Fig. 5 for upstream and downstream source configurations (in red and blue respectively) and are compared to the configuration without acoustic excitation in black. The streamwise location x/L increases from left to right.

At the leading edge of the liner ($x/L \approx 0.01$), the mean velocity profiles remain essentially identical to the baseline case for both configurations. This observation indicates that the mere presence of a grazing acoustic wave does not directly affect the mean flow over the rigid surface upstream of the liner.

Farther downstream, a clear deficit of the mean streamwise velocity appears in the near-wall region. At $x/L \approx 0.58$, a reduction of the mean velocity is observed for $y/h \lesssim 0.1$, while the outer part of the boundary layer remains unaffected. This deficit becomes more pronounced toward the trailing edge ($x/L \approx 0.99$), indicating a cumulative effect of the acoustic-liner interaction as the flow develops over the lined section. At the end of the lined section, similar mean-flow distributions are observed for the two acoustic source configurations, although both remain markedly below the baseline profile. The slight near-wall velocity deficit observed in the presence of acoustic forcing suggests a modification of the momentum balance within the boundary layer. The oscillatory velocity field associated with the grazing acoustic wave introduces an additional unsteady shear near the wall, which may enhance momentum exchange and contribute to a redistribution of the mean velocity profile. Similar near-wall modifications of the mean flow have been reported in studies of turbulent flow over perforated plates and acoustic liners [15, 28], and have been observed to become more pronounced under acoustic excitation [14, 16].

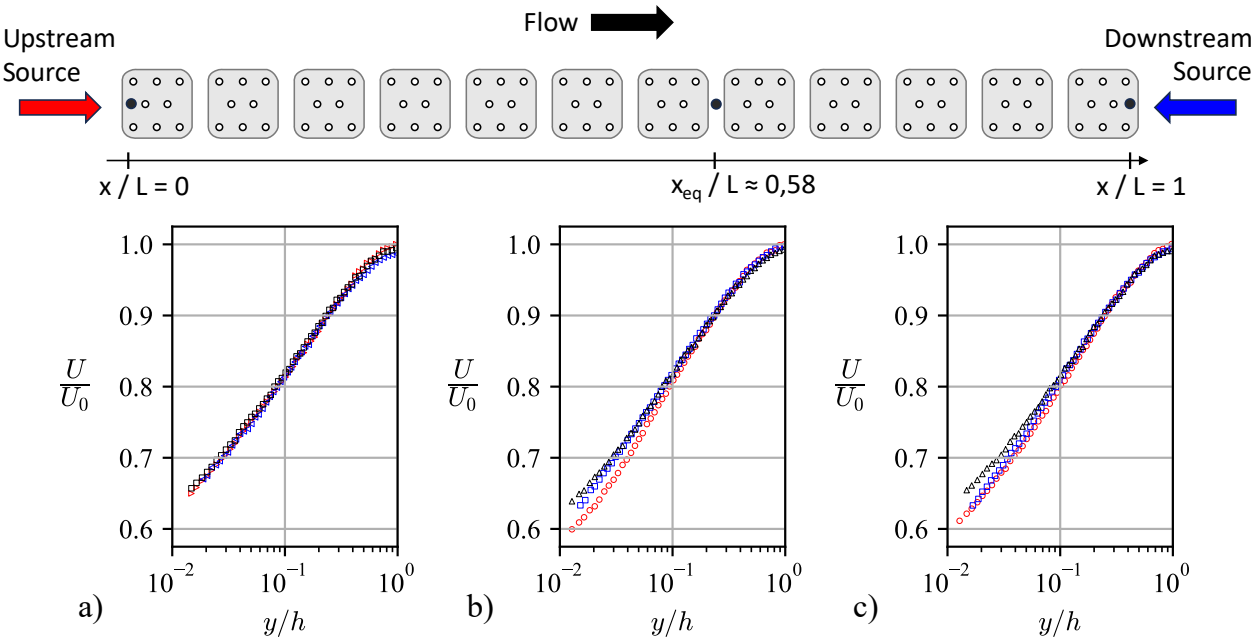

Fig. 5 Mean streamwise velocity profiles under acoustic forcing for upstream and downstream source configurations (upstream in red. downstream in blue and no acoustic in black).

The magnitude of the mean velocity deficit varies with streamwise location and depends on the acoustic source position. For upstream excitation, the reduction in mean velocity is stronger over the first half of the liner and weakens downstream, whereas for downstream excitation the deficit increases toward the trailing edge. This opposite streamwise evolution mirrors the acoustic attenuation along the liner reported in the acoustic characterization section (cf. Fig. 3b), suggesting that the observed mean-flow modification is closely linked to the local acoustic forcing amplitude. These observations are consistent with the recent numerical results reported by Paduano et al. [16]. At the end of the liner, the mean velocity profiles obtained for the upstream and downstream configurations become very similar. This behavior suggests that the flow progressively adapts to the perturbations induced by the grazing acoustic wave.

C. Modification of second-order statistics

The previous sections have shown that grazing acoustic excitation over the liner induces a localized modification of the mean flow, characterized by a reduction of the streamwise velocity in the near-wall region. In addition, the analysis of the baseline case highlighted modifications of the velocity second-order statistics induced by the presence of the liner. We now examine the associated changes in the presence of acoustic excitation in order to quantify the impact of the acoustic forcing on velocity fluctuations and to determine the spatial extent of the interaction region.

Figure 6 presents the wall-normal profiles of the velocity fluctuation variance, u^2_{rms}/U^2_0 and v^2_{rms}/U^2_0, at three representative streamwise locations along the liner, with increasing x/L from left to right. Results obtained without acoustic excitation are used as a reference.

When grazing acoustic excitation is applied, marked differences appear along the liner in both velocity components compared to the configuration without acoustics. At the leading edge of the liner ($x/L \approx 0.01$), no significant modification of the fluctuation levels is observed, indicating that the grazing acoustic waves have a low impact on the turbulent boundary layer over the rigid surface before the liner.

At $x/L \approx 0.58$, a distinct increase of both u^2_{rms}/U^2_0 and v^2_{rms}/U^2_0 fluctuations is observed for $y/h \lesssim 0.1$. This enhancement is more pronounced for upstream acoustic excitation, which is consistent with the higher local acoustic amplitudes measured in the first part of the liner for this configuration (cf. Fig. 3b). Farther away from the wall, the fluctuation levels remain close to the reference case, indicating that the acoustic impact is spatially confined.

Towards the trailing edge ($x/L \approx 0.99$), the enhancement of velocity fluctuations intensifies for the downstream case, remaining predominantly confined to the near-wall region. The upstream case presents an opposite trend with a

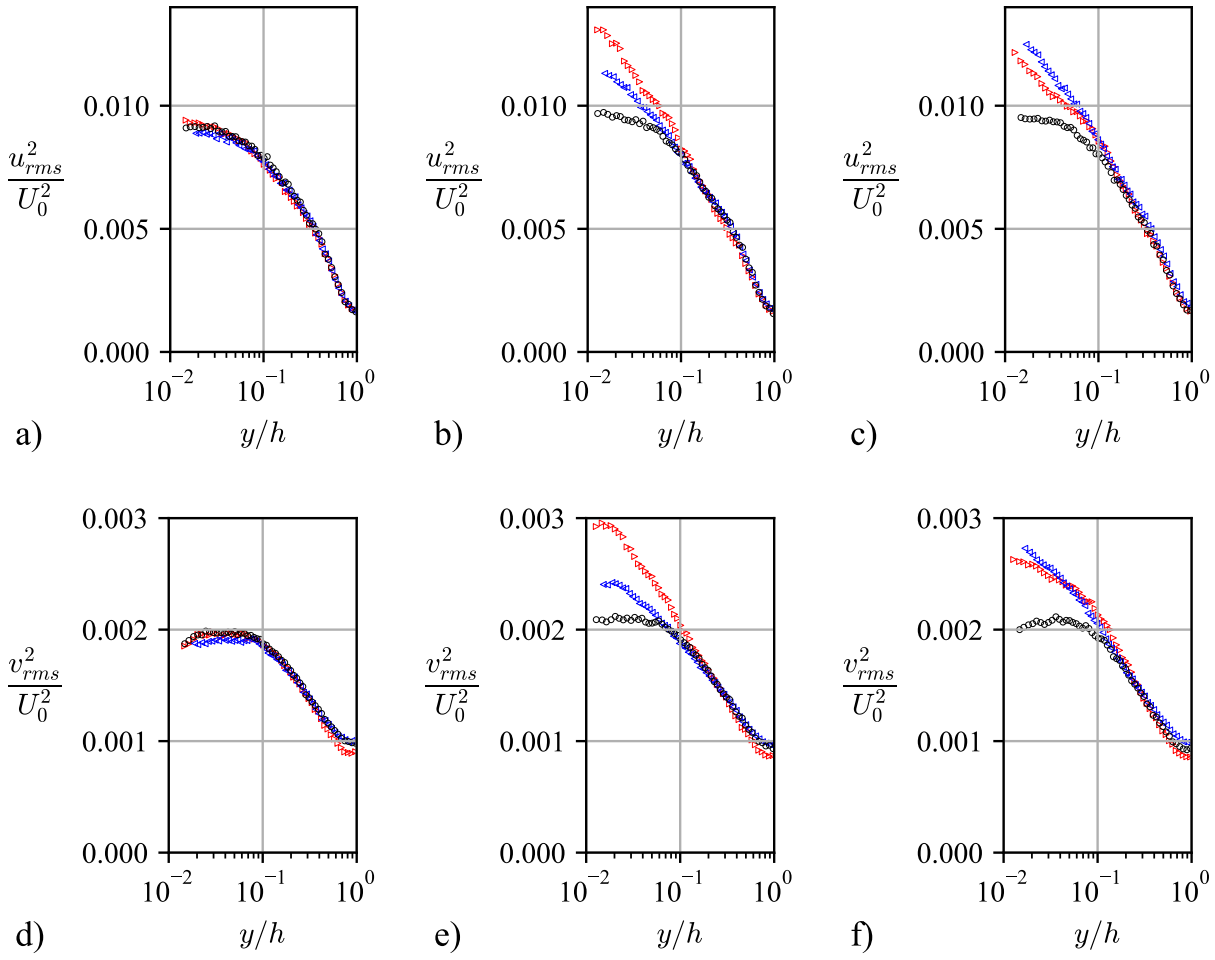

Fig. 6 Streamwise (top) and wall-normal (bottom) velocity fluctuation variances under acoustic forcing (upstream in red, downstream in blue and baseline in black) at three streamwise locations.

slight reduction compared to the previous x-location. This trend is consistent with the decrease of acoustic amplitude along the liner in the upstream configuration, suggesting that the fluctuation levels are primarily driven by the local acoustic forcing.

At this location, downstream acoustic excitation leads to stronger fluctuation levels than upstream excitation, reflecting the inversion of the acoustic amplitude distribution along the liner. These observations suggest that the development of turbulent fluctuations is more strongly linked to the local acoustic forcing than to the global excitation level alone. This trend is consistent with the stronger SPL decay observed along the liner for the downstream source.

The wall-normal profiles of the streamwise and wall-normal velocity fluctuations reveal the emergence of a localized region of enhanced turbulent activity when grazing acoustic excitation is applied. This region is consistently observed in the near-wall zone, typically for $y/h \lesssim 0.1$, and coincides with the wall-normal location where the most significant deficit of the mean streamwise velocity was reported in the previous section.

Both velocity components exhibit an increase of fluctuation levels within this region; however, the response of the wall-normal component is more strongly confined to the vicinity of the liner surface than that of the streamwise component. Away from the wall, the fluctuation levels remain close to the baseline case, indicating that the acoustic forcing primarily affects a limited portion of the boundary layer.

As discussed in Section V.A, the present LDV measurements do not extend sufficiently close to the wall to capture the inner peak of the turbulence intensity commonly reported in the literature [15, 16, 28, 30]. The observed enhancement of velocity fluctuations within the accessible region therefore suggests a redistribution of turbulent activity within the

boundary layer rather than a uniform amplification across the entire profile.

This redistribution appears to be associated with the mean velocity deficit discussed previously. In the vicinity of the liner surface, the presence of the perforations promotes wall-normal transport associated with the exchange of fluid between the grazing flow and the orifice cavities. Under acoustic forcing, this mechanism may be further amplified by the oscillatory motion induced by the grazing acoustic wave. The periodic forcing at the perforation edges may generate localized disturbances in the boundary layer, potentially promoting enhanced turbulent mixing. The resulting interaction between acoustic forcing and turbulent structures may contribute to the amplification of second-order statistics observed within the measured portion of the boundary layer.

The magnitude and streamwise evolution of the fluctuation enhancement depend on the acoustic source position and therefore on the local acoustic forcing amplitude along the liner. Regions subjected to higher local acoustic amplitudes exhibit the most significant increases of both u' and v' fluctuations, together with a more pronounced modification of the mean flow, consistent with the numerical study of Paduano et al. [16].

VI. Spectral analysis of the velocity fluctuation

The previous sections have demonstrated that grazing acoustic excitation over the liner leads to a localized reduction of the mean streamwise velocity and a significant enhancement of velocity fluctuations in the near-wall region. These effects are modulated by the streamwise location along the liner and the acoustic source position.

In order to further characterize the underlying mechanisms and identify the turbulent scales affected by the acoustic forcing, this section examines the spectral redistribution of the velocity fluctuations. The analysis focuses on the premultiplied power spectral density, $fS_{u'u'}$ and $fS_{v'v'}$, with f the frequency and S_{ii} the PSD of the component i.

A. Spectral Redistribution of Streamwise Velocity Fluctuation

Figure 7 presents four colormaps of the premultiplied PSD for the streamwise component. From left to right, PSDs are extracted from velocity profiles measured at the leading and trailing edges of the liner. The top row corresponds to the upstream configuration and the bottom row to the downstream configuration.

For both configurations, a broadband increase in spectral energy is observed as the flow develops along the liner, consistent with the enhancement of velocity fluctuations reported in the previous section. This increase in spectral energy is mainly confined to the near-wall region, typically for $y/h \lesssim 0.1$. This result is in agreement with the findings of Hoang et al. [30] attributing this turbulence promotion to a redistribution of turbulent energy from the near-wall region toward the outer region.

In addition to the broadband response, a distinct tonal contribution is visible at the excitation frequency f_e. For upstream excitation, this tonal signature appears more marked at the leading edge than the trailing edge, indicating a progressive attenuation of the acoustic component along the liner.

Conversely, for downstream excitation, the same tonal signature is observed at the trailing edge, decreasing toward the leading edge and reaching a lower level than in the upstream configuration after propagating over the entire liner. This opposite behavior is fully consistent with the measured evolution of the sound pressure level along the liner reported in the acoustic characterization section IV.

The impact of the acoustic source location is not observable on the rest of the spectrum as both configurations provide a similar broadband increase. A direct comparison of the two configurations is not relevant at these positions, as the difference is more pronounced at the x_{eq} location than at the leading and trailing edge locations, as observed in the previous sections. Subsection VI.C is dedicated to the comparison of the spectral content at the x_{eq} location for upstream and downstream configurations.

B. Spectral Redistribution of Wall-Normal Velocity Fluctuation

Figure 8 presents four colormaps of the premultiplied PSD for the wall-normal component. From left to right, PSDs are extracted from the profile at the leading or trailing edge of the liner. The top row corresponds to the upstream configuration and the bottom row to the downstream configuration.

Two major differences are observed in comparison to the spectral distribution of the streamwise fluctuating velocity. First, as expected for a wall-bounded flow, and observed in section V.C, the energy of the wall-normal velocity fluctuations is lower than that of the streamwise component. In addition, the dominant frequency band also differs, with the largest wall-normal fluctuation energy occurring at frequencies above approximately 1000 Hz.

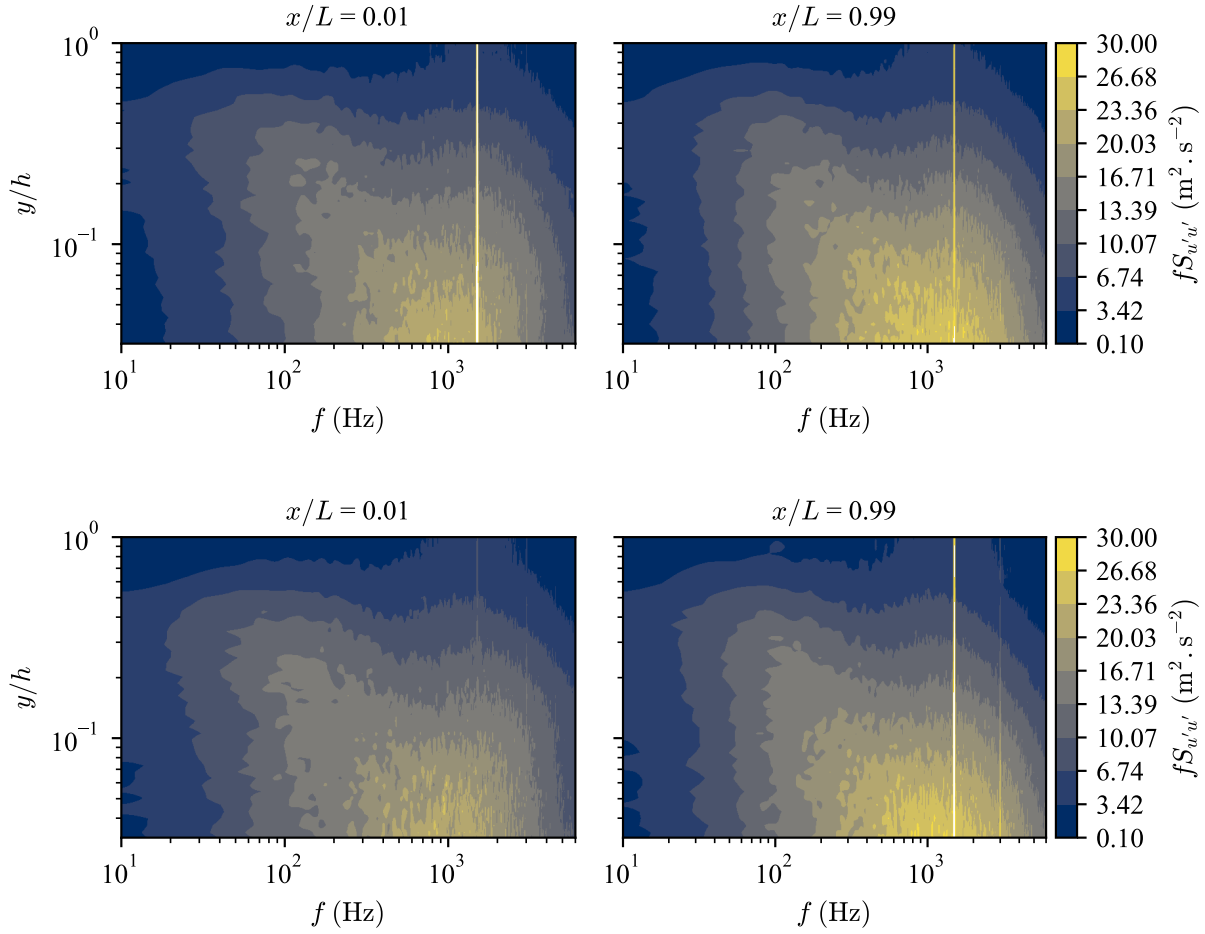

Fig. 7 Premultiplied PSD of streamwise velocity fluctuations at leading and trailing edge locations for upstream (top) and downstream (bottom) source configurations.

From the leading edge to the trailing edge, the spectral differences are primarily observed in this frequency band, with a local increase mainly confined to the near-wall region.

The narrow band associated with the coherent acoustic wave at frequency f_e is less clearly visible, but it remains detectable and indicates deviations from a purely plane acoustic wave. In the downstream case, it almost never emerges from the non-coherent turbulent fluctuation energy. This highlight that even at the same incident level, the contrast between the amplitude of the wall-normal acoustic-induced velocity and the amplitude of the non-coherent part of the signal is reduced for the downstream source configuration. These results will be further commented in section VII on the acoustic-induced velocity amplitude at the forcing frequency.

C. Spectral distribution of fluctuating velocity energy near the surface of the liner

This section focuses on the impact of the acoustic source location on the near-wall fluctuating energy. Fig. 9 presents the PSD of the two velocity fluctuation components measured at a representative location over the liner. To remain consistent with the previous analysis, the spectra are shown at the streamwise location $x_{eq}/L = 0.58$ and at a wall-normal distance of $y/h \approx 0.02$, which corresponds to the closest measurement point to the liner surface available in both acoustic configurations. At this location, significant differences in velocity fluctuation variance were previously observed.

First, a clear narrow energy peak is observed at the excitation frequency f_e in both acoustic configurations in the spectrum $S_{u'u'}$. This peak corresponds to the coherent acoustic component emerging from the broadband turbulent

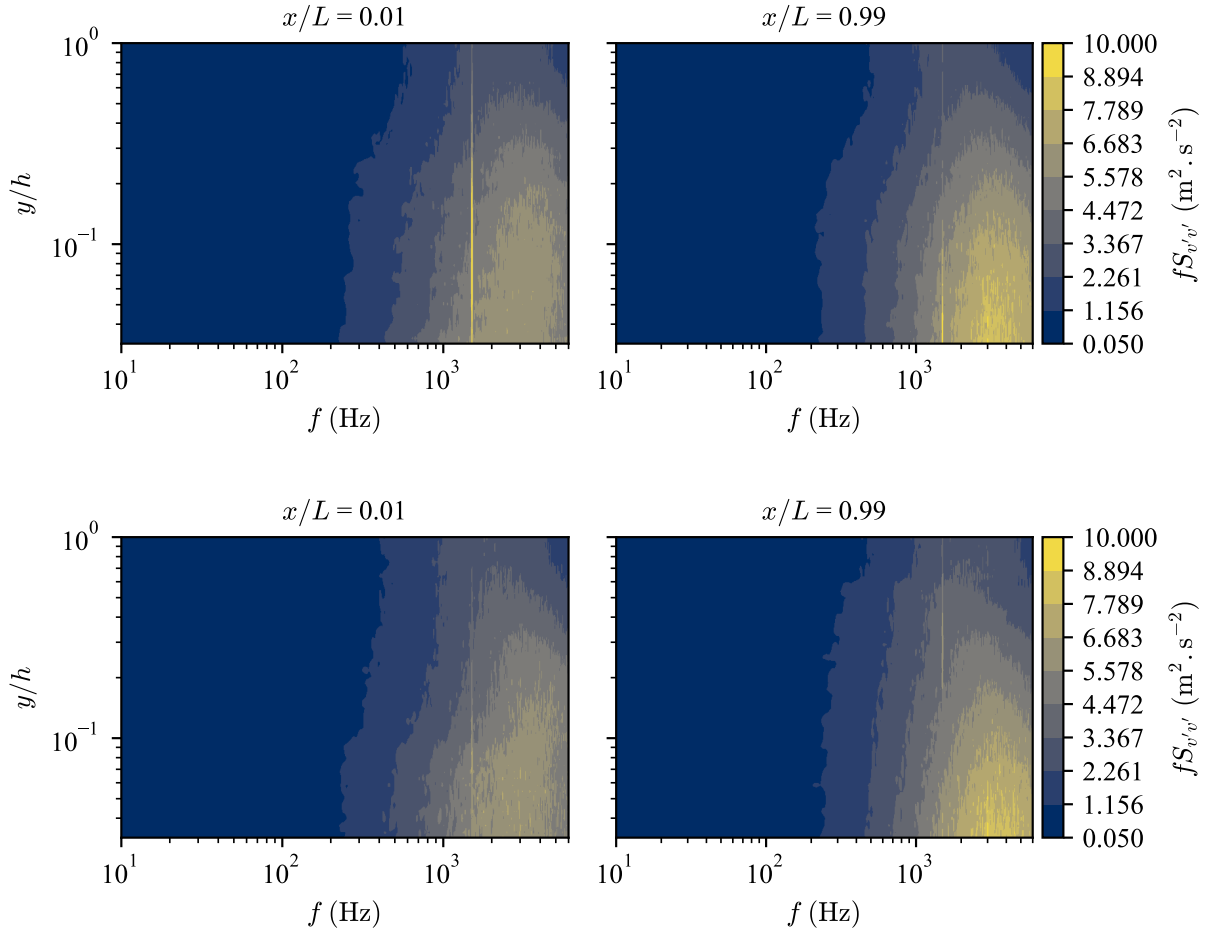

Fig. 8 Premultiplied PSD of wall-normal velocity fluctuations at leading and trailing edge locations for upstream (top) and downstream (bottom) source configurations.

fluctuations. The first harmonic is also visible at 3000 Hz. The influence of the acoustic source location is already apparent in the amplitude of the coherent peak, which is higher for the upstream configuration. This observation indicates a strong modulation of the acoustic-induced velocity amplitude near the liner surface, even at the streamwise location where the acoustic pressure measured on the opposite wall yields similar SPL values in the two source configurations.

Outside the coherent contribution, differences between the configurations are also observed in the broadband part of the spectrum, particularly at high frequencies. In the upstream source configuration, a broadband increase of spectral energy is observed compared with the baseline case, suggesting an enhanced interaction between the strong acoustic forcing and the turbulent boundary layer. In contrast, in the downstream source configuration the spectral amplitude remains close to the baseline case, except at frequencies below 300 Hz where it becomes comparable to the upstream case. This behavior is consistent with the lower acoustic amplitude encountered by the turbulent flow over the first part of the liner in the downstream configuration.

Similar trends are observed for the wall-normal velocity component, although the differences between the configurations at low frequencies are more pronounced.

These observations highlight the influence of the acoustic source location on the local turbulent dynamics above the liner. While the overall flow development along the liner eventually becomes similar for both configurations, significant local differences in the fluctuating velocity field are observed in the near-wall region. These results indicate that the turbulent boundary layer experiences different acoustic forcing histories depending on the propagation direction of the acoustic wave, which leads to locally different turbulent responses above the liner.

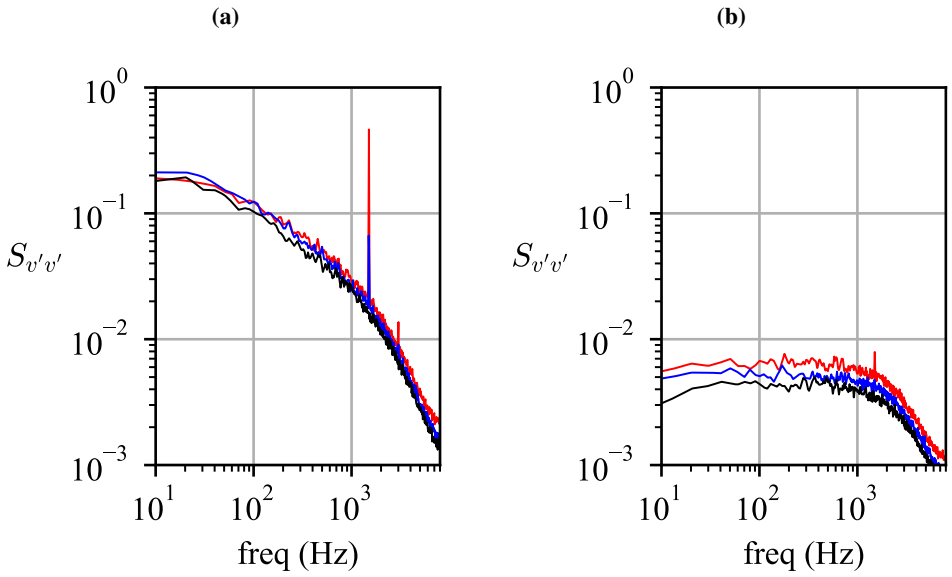

Fig. 9 Velocity fluctuation spectra near the liner surface at x_{eq}/L = 0.58 for both acoustic for upstream (red) and downstream (blue) source configurations.

VII. Acoustic-induced velocity field above the lined section

The previous sections have established that the modification of the mean flow, turbulence intensities, and spectral content is governed by the local acoustic forcing along the liner. To complete the description of these interactions, this subsection examines how the acoustic wave itself evolves through its interaction with the turbulent boundary layer.

The amplitude of acoustic-induced velocity at the forcing frequency f_e is denoted $|\tilde{u}_{ac}|$ and $|\tilde{v}_{ac}|$ for the streamwise and wall-normal directions, respectively. Fig. 10 presents wall-normal profiles of these components at three representative streamwise locations along the liner for upstream and downstream excitation configurations. From left to right, the plots follow the acoustic propagation from the inlet to the outlet either with the flow or against the flow. Note that the definition of the inlet and outlet locations depends on the direction of acoustic propagation, as detailed in Table 3.

Table 3 Locations in regard of the acoustic propagation in the two acoustic source configurations.

Configuration	locations	inlet	x_{eq}	outlet
Upstream	x/L	0.01	0.58	0.99
Downstream	x/L	0.99	0.58	0.01

The streamwise acoustic-induced velocity $|\tilde{u}_{ac}|$ exhibits clear distortions within the near-wall region above the liner. At the entrance of the lined section (Fig. 10a), the two excitation configurations already display slight differences close to the wall, while the profiles remain similar farther from the surface. As the acoustic wave propagates along the liner, these differences progressively increase. At x_{eq} (Fig. 10b), the divergence between the two configurations becomes more pronounced, indicating that the boundary layer developing over the liner progressively modifies the structure of the propagating acoustic field. The local peak observed at $y/h \approx 0.2$ corresponds to the coherent acoustic contribution identified in the spectral analysis. This behavior persists toward the trailing edge (Fig. 10c). Along the liner, $|\tilde{u}_{ac}|$ undergoes a gradual attenuation that follows the SPL decay measured with microphones (cf Fig. 3b), with the increased attenuation in the downstream configuration.

The wall-normal acoustic-induced velocity $|\tilde{v}_{ac}|$ provides a clearer signature of this interaction. In both configurations, significant wall-normal acoustic motion develops within the boundary-layer region and varies markedly along the liner. At the liner entrance (Fig. 10d), the two source locations already generate distinct responses. These differences become less pronounced at x_{eq} (Fig. 10e), where the wall-normal acoustic velocity shape tend to be similar for the two acoustic source configurations. This similarity does not stand toward the liner exit (Fig. 10f), where strong differences re-appear

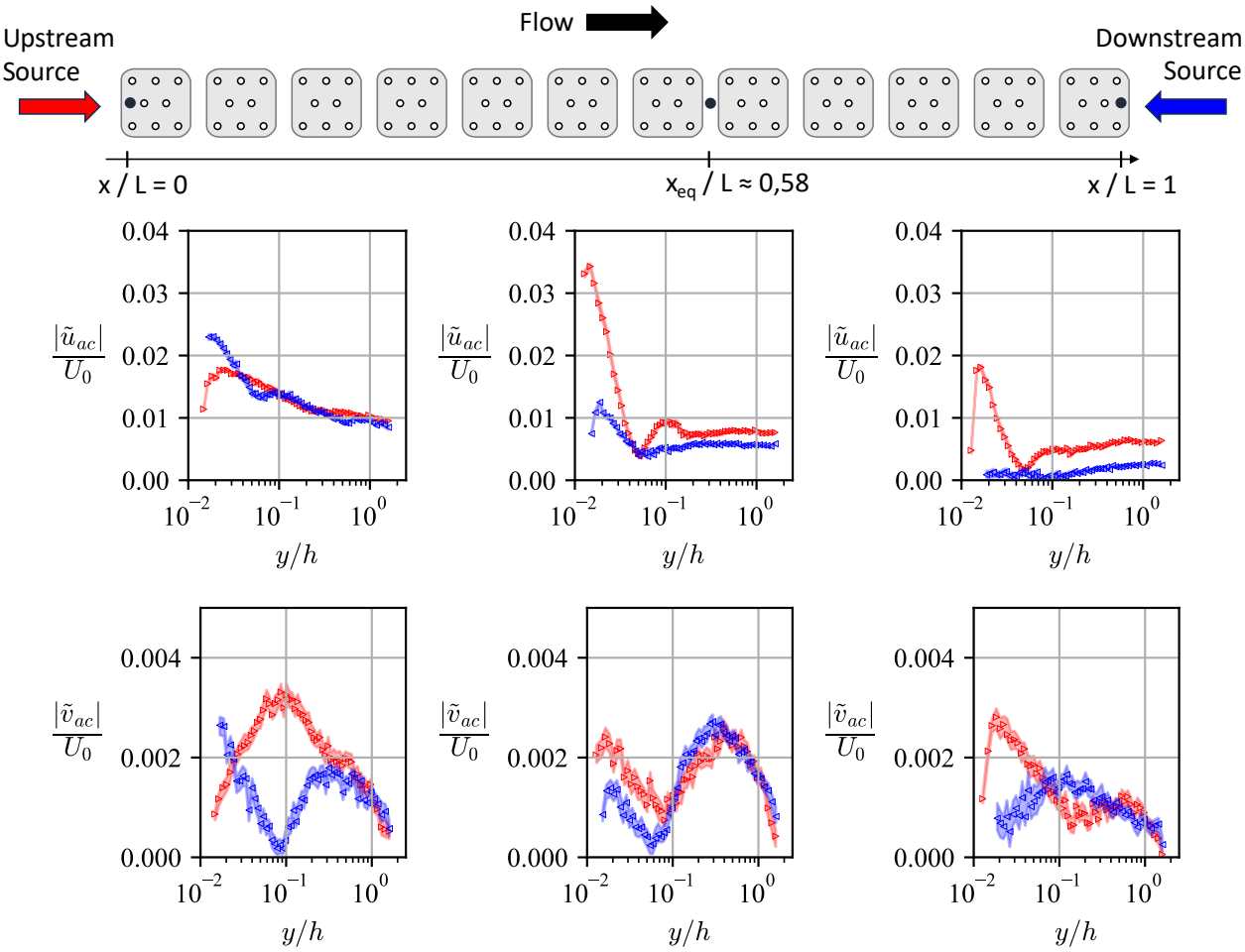

Fig. 10 Streamwise (top) and wall-normal (bottom) acoustic-induced velocity amplitudes along the liner for upstream (red) and downstream (blue) source configurations.

in the profile. At the selected streamwise locations, it is likely that the wall-normal acoustic-induced velocity amplitude profiles are shaped by the proximity of the perforation orifices. The resulting wall-normal motion may contribute to the momentum redistribution observed in the near-wall region ($y/h \lesssim 0.1$).

The presence of a measurable wall-normal acoustic-induced velocity component highlights the three-dimensional nature of the acoustic–flow interaction near the liner surface. While the incident acoustic wave primarily propagates in the streamwise direction, its interaction with the turbulent boundary layer and with the impedance boundary condition imposed by the liner appears to induce a local redistribution of acoustic particle velocity. This produces a non-negligible wall-normal velocity component within the near-wall region, reflecting the complex coupling between the acoustic field and the boundary layer dynamics.

Significant differences are observed between the upstream and downstream acoustic forcing configurations. These differences arise from the distinct spatial distributions of the acoustic field along the liner and from the relative propagation direction of the acoustic wave with respect to the mean flow. When the acoustic source is located upstream, the acoustic wave interacts progressively with the developing boundary layer as it propagates over the liner. In contrast, downstream forcing interacts with a more developed boundary layer, which may lead to a different coupling between the acoustic field and the convecting turbulent structures, resulting in a different local flow–acoustic response. These effects highlight the importance of the acoustic propagation direction when analyzing grazing flow–liner interactions.

These observations suggest that the interaction between the acoustic field and the turbulent boundary layer involves a two-way coupling mechanism, where the acoustic wave modifies the turbulence structure while the turbulent flow simultaneously alters the local acoustic velocity field.

VIII. Conclusions

Time-resolved Laser Doppler Velocimetry (LDV) measurements were performed to investigate the interaction between a turbulent boundary layer and a grazing acoustic wave over a multi-orifice SDOF liner. The study characterized modifications of the mean velocity field, second-order statistics, and spectral content of the velocity fluctuations, with particular emphasis on the influence of the acoustic source position.

Even in the absence of acoustic forcing, the turbulent boundary layer adapts to the liner surface primarily through a localized increase in turbulence intensity in the near-wall region ($y/h \lesssim 0.1$). This increase is attributed to a redistribution of turbulent activity within the boundary layer. In contrast, the mean velocity field remains largely unchanged within the accessible measurement region, indicating that the aerodynamic influence of the liner on the outer boundary-layer structure is limited.

Under acoustic excitation, the flow response becomes strongly localized near the wall ($y/h \lesssim 0.1$). A deficit in the mean streamwise velocity develops along the liner and is accompanied by an increase in velocity fluctuations, particularly in the wall-normal component. The outer region of the boundary layer remains largely unaffected, indicating that the interaction between the grazing acoustic wave and the turbulent boundary layer primarily modifies near-wall transport processes.

A central outcome of the study is the strong dependence of the aerodynamic response on the acoustic source position. Although the global excitation level is maintained, upstream and downstream forcing generate different spatial distributions of acoustic amplitude along the liner. The magnitude and streamwise evolution of the flow modifications consistently follow the local acoustic attenuation, demonstrating that the aerodynamic response is governed by the spatial distribution of the acoustic forcing.

Spectral analysis further reveals a broadband redistribution of non-coherent energy toward higher frequencies, together with a distinct coherent contribution at the excitation frequency. The spatial evolution of this tonal component follows the distribution of the acoustic-induced velocity field, establishing a direct link between coherent acoustic forcing and the modification of turbulent fluctuations.

The analysis of the acoustic-induced velocity field constitutes a central contribution of the present study. Using time-resolved LDV measurements, it is possible to directly extract the coherent acoustic velocity components within a turbulent boundary layer, providing experimental access to the local structure of the acoustic field in the immediate vicinity of the liner. The results reveal significant distortions of both streamwise and wall-normal acoustic velocity components within the near-wall region, with increasing differences between upstream and downstream configurations along the liner. In particular, the emergence of a non-negligible wall-normal acoustic velocity component highlights the redistribution of acoustic particle motion induced by the interaction with the turbulent boundary layer and the impedance boundary condition. The spatial evolution of these components follows the measured attenuation of the acoustic field, demonstrating that the boundary layer not only responds to the acoustic forcing but also actively modifies the structure of the propagating wave. These observations provide direct experimental evidence of the feedback of turbulence on the acoustic field under grazing flow conditions.

Although the measurements do not resolve the viscous sublayer, the results provide detailed experimental evidence that liner–flow interaction under grazing acoustics is highly localized and strongly controlled by the spatial evolution of the acoustic field. Furthermore, the propagation direction of the acoustic wave relative to the mean flow significantly influences the local aerodynamic response. These observations highlight the presence of a two-way coupling mechanism in which the acoustic field modifies the turbulence structure while the turbulent boundary layer simultaneously alters the local acoustic velocity field.

These findings provide new experimental insight into acoustic–turbulence coupling mechanisms in lined ducts and offer valuable data for the development and validation of improved impedance models under grazing flow conditions. In particular, the results suggest that accounting for turbulence effects during impedance eduction may help explain discrepancies observed between impedances educed using upstream and downstream acoustic sources.

Future work will focus on refining the spatial resolution of the measurements in the vicinity of the liner perforations in order to investigate the local flow dynamics associated with the orifice-scale acoustic response. In particular, measurements performed at different spanwise locations relative to the perforation pattern will enable the characterization of local variations of the velocity field induced by the oscillatory mass flow through the orifices. Additional investigations involving more complex liner geometries and longer samples are also planned to further clarify the role of turbulence statistics in shaping the effective acoustic response of liners under grazing flow conditions.

Appendix

A. Impact of the Bias-filtering procedure

A bias-filtering procedure was applied to the velocity measurements in order to remove a systematic offset observed in some of the raw LDV signals. The procedure relies on a bandwidth velocity filter applied prior to the calibration rotation and resampling procedure described in Sec. III.f.

Because such post-processing may potentially alter the statistical properties of the signal, the impact of the procedure on the velocity statistics was evaluated using measurements known to be free of bias.

1. Description of the bias and correction method

The LDV measurements exhibited a localized nonphysical accumulation of samples in one velocity component acquired before applying the calibration rotation matrix R_M,

$$\begin{pmatrix} u \\ v \end{pmatrix} = R_M \begin{pmatrix} B \\ G \end{pmatrix} \tag{9}$$

here denoted B and G for the blue and green pair of beams. The accumulation appeared localized in a narrow interval $[G\text{min}, G\text{max}]$ as represented in Figure 11. This feature was identified as an acquisition bias associated with a retro-diffusion effect happening on the path of the pair of beams. Because the bias affects only a narrow and well-identified velocity range, a local sample-rejection strategy was preferred over a global filtering procedure. This approach minimizes the alteration of the measured signal while removing the clearly nonphysical contribution.

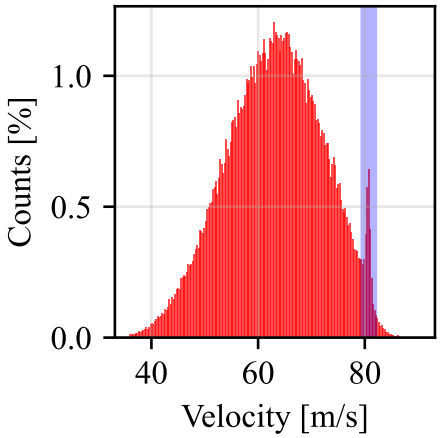

Fig. 11 Histogram of velocity distribution illustrating the bias-filtering interval applied to LDV measurements between 79 and 82 m/s.

For each measurement, a mask was defined as

$$\mathcal{M} = \{\, i \mid G_i < G_{\text{min}} \;\text{ or }\; G_i > G_{\text{max}} \,\}, \tag{10}$$

so that all samples lying inside the artifact interval were discarded. The same mask was applied consistently to the time series, velocity components, and auxiliary analog signals, yielding the cleaned datasets

$$t^{\text{clean}} = t(\mathcal{M}), \qquad \mathbf{u}^{\text{clean}} = \mathbf{u}(\mathcal{M}), \qquad \mathbf{s}^{\text{clean}} = \mathbf{s}(\mathcal{M}). \tag{11}$$

The rejection procedure has been implemented prior to the uniform temporal grid resampling using linear interpolation for each measured points. This resampling step is standard in LDV signal processing and is required for the computation of spectral quantities such as power spectral densities obtained through Fourier analysis. In the mean time, this resampling cover the artificial gap created in the interval $[G_{\text{min}}, G_{\text{max}}]$.

2. Evaluation of the Correction Impact

To evaluate the effect of the sample rejection procedure, the algorithm was applied to velocity profiles that do not contain the bias. Any modification of the flow statistics therefore corresponds to an error introduced by the sample rejection itself.

For each velocity statistic q, the relative error introduced by the sample rejection was computed as

$$\varepsilon_q = \frac{q_{\mathrm{corr}} - q_{\mathrm{ref}}}{q_{\mathrm{ref}}}, \tag{12}$$

where q_{ref} denotes the reference statistic obtained from the original measurements and q_{corr} the statistic obtained after applying the sample rejection procedure.

Figure 12 shows the relative error introduced by the sample rejection algorithm for the velocity statistics. The top row presents the error in the mean velocity components U_{mean} and V_{mean} normalized by U_{mean}, while the bottom row shows the error in the velocity fluctuations u_{rms} and v_{rms}.

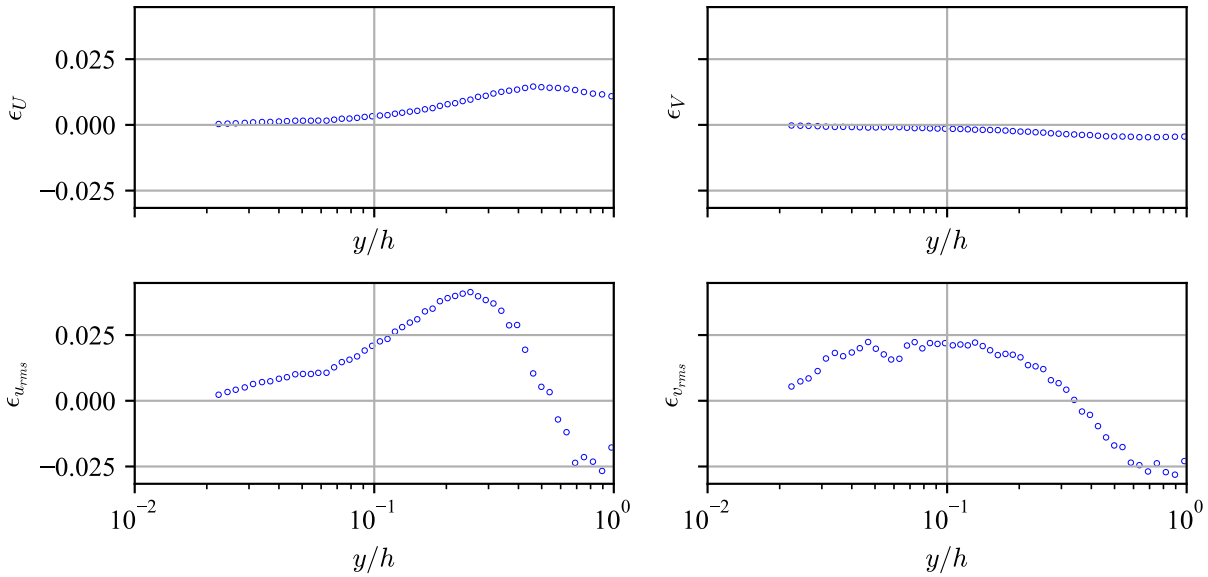

Fig. 12 Relative error in velocity statistics induced by the bias-filtering procedure along the wall-normal direction.

The error in U_{mean} remains below approximately 2% over the entire profile, while the error in V_{mean} remains negligible. Slightly larger deviations are observed for the fluctuation statistics, with maximum errors of approximately 4% for u_{rms} and 2% for v_{rms} in the outer region of the flow.

The filtering procedure produces a systematic one-sided effect on the velocity statistics. In all cases, the procedure results in a slight reduction of the mean and rms velocity values. In the spectral domain, this behavior manifests as a broadband attenuation of the spectral energy, rather than a frequency-localized modification. This systematic decrease reflects the removal of spurious high-energy samples associated with the corrupted data.

Overall, the errors introduced by the sample rejection procedure remain small compared with the magnitude of the measured quantities and with the variations observed in the flow statistics. The sample rejection procedure therefore does not significantly alter the physics discussed in the study and has been deemed usable in this context.

Declaration of Generative AI and AI-assisted technologies in the writing process

During the preparation of this work the authors used ChatGPT in order to improve language and readability. After using this tool, the authors reviewed and edited the content as needed and take full responsibility for the content of the publication.

Declaration of competing interest

The authors have no conflict of interest to declare.

Acknowledgments

The work of L. Ambrosiani is co-funded by ONERA and the European Union (ERC, LINING, 101075903). The work of F. Avallone is co-funded by the European Union (ERC, LINING, 101075903). Views and opinions expressed are however those of the author(s) only and do not necessarily reflect thoe of the European Union or the European Research Council. Neither the European Union nor the granting authority can be held responsible for them. The authors thanks the AeroAcoustics Research Consortium (AARC) for sharing the liner geometry. The AARC is a government-industry partnership supporting pre-competitive research for aircraft noise reduction. The authors are grateful to Nicolas Fasano and Laurent Burel for their help in setting up the LDV flow seeder and manufacturing the liner sample, respectively, and to Rémi Roncen and Victor Lafont for fruitful discussions.

References

[1] Motsinger, R. E., and Kraft, R. E., "Design and Performance of Duct Acoustic Treatment," *Aeroacoustics of Flight Vehicles: Theory and Practice, Volume 2: Noise Control*, NASA Langley Research Center, 1991.

[2] Hughes, C., "The Promise and Challenges of Ultra High Bypass Ratio Engine Technology and Integration," *AIAA Aero Sciences Meeting*, 2011, pp. 0–11.

[3] Casalino, D., Hazir, A., and Mann, A., "Turbofan broadband noise prediction using the lattice Boltzmann method," *AIAA Journal*, Vol. 56, No. 2, 2018.

[4] Jones, M., Simon, F., and Roncen, R., "Broadband and Low-Frequency Acoustic Liner Investigations at NASA and ONERA," *AIAA Journal*, Vol. 60, 2022, pp. 1–20. https://doi.org/10.2514/1.J060862.

[5] Ma, X., and Su, Z., "Development of Acoustic Liner in Aero Engine: A Review," *Science China Technological Sciences*, Vol. 63, No. 12, 2020, pp. 2491–2504. https://doi.org/10.1007/s11431-019-1501-3.

[6] Avallone, F., Paduano, A., Pereira, L. M., Bonomo, L. A., Cordioli, J. A., Casalino, D., and Cerizza, D., "On the comparison of different methods for impedance eduction applied to a numerical database," *30th AIAA/CEAS Aeroacoustics Conference*, 2024.

[7] Bonomo, L. A., Quintino, N., Cordioli, J. A., Avallone, F., Jones, M. G., Howerton, B. M., and Nark, D. M., "A Comparison of Impedance Eduction Test Rigs with Different Flow Profiles," *AIAA AVIATION 2023 Forum*, 2023.

[8] Brambley, E. J., "Well-posed boundary condition for acoustic liners in straight ducts with flow," *AIAA Journal*, Vol. 49, No. 6, 2011, pp. 1272–1282.

[9] Rienstra, S. W., and Darau, M., "Boundary-layer thickness effects of the hydrodynamic instability along an impedance wall," *Journal of Fluid Mechanics*, Vol. 671, 2011, pp. 559–573.

[10] Roncen, R., Piot, E., Mery, F., Simon, F., Jones, M., and Nark, D., "Wavenumber-Based Impedance Eduction with a Shear Grazing Flow," *AIAA Journal*, Vol. 58, 2020, pp. 1–11. https://doi.org/10.2514/1.J059100.

[11] Roncen, R., Méry, F., Piot, E., and Klotz, P., "Spatially-Varying Impedance Model for Locally Reacting Acoustic Liners at a High Sound Intensity," *Journal of Sound and Vibration*, Vol. 524, 2022, p. 116741. https://doi.org/10.1016/j.jsv.2021.116741.

[12] Renou, Y., and Aurégan, Y., "Failure of the Ingard-Myers Boundary Condition for a Lined Duct: An Experimental Investigation," *The Journal of the Acoustical Society of America*, Vol. 130, No. 1, 2011, pp. 52–60. https://doi.org/10.1121/1.3586789.

[13] Zhang, Q., and Bodony, D. J., "Numerical investigation of a honeycomb liner grazed by laminar and turbulent boundary layers," *Journal of Fluid Mechanics*, Vol. 792, 2016, pp. 936–980.

[14] Léon, O., Mery, F., Piot, E., and Conte, C., "Near-Wall Aerodynamic Response of an Acoustic Liner to Harmonic Excitation with Grazing Flow," *Experiments in Fluids*, Vol. 60, 2019. https://doi.org/10.1007/s00348-019-2791-5.

[15] Shahzad, H., Hickel, S., and Modesti, D., "Turbulence and added drag over acoustic liners," *Journal of Fluid Mechanics*, Vol. 965, 2023.

[16] Paduano, A., Scarano, F., Cordioli, J., Casalino, D., and Avallone, F., "On the impact of the turbulent grazing flow development on the acoustic response of an acoustic liner," *arXiv*, 2025. https://doi.org/10.48550/arXiv.2507.22714, URL https://arxiv.org/abs/2507.22714, preprint.

[17] Avallone, F., Manjunath, P., Ragni, D., and Casalino, D., "Lattice-Boltzmann very large eddy simulation of a multi-orifice acoustic liner with turbulent grazing flow," *25th AIAA/CEAS Aeroacoustics Conference*, 2019.

[18] Quintino, N. T., Bonomo, L. A., Cordioli, J. A., Jones, M. G., Howerton, B. M., Nark, D. M., and Avallone, F., "Comparison of Impedance Eduction Test Rigs with Different Boundary-Layer Profiles," *AIAA Journal*, 2025, pp. 1–12. https://doi.org/10.2514/1.J065173.

[19] Lafont, V., Méry, F., Roncen, R., Simon, F., and Piot, E., "Liner Impedance Eduction Under Shear Grazing Flow at a High Sound Pressure Level," *AIAA Journal*, Vol. 58, No. 3, 2020, pp. 1107–1117. https://doi.org/10.2514/1.J058756, URL https://doi.org/10.2514/1.J058756.

[20] Bonomo, L. A., Quintino, N. T., Spillere, A. M., Cordioli, J. A., and Murray, P. B., "A Comparison of In-Situ and Impedance Eduction Experimental Techniques for Acoustic Liners with Grazing Flow and High SPL," *28th AIAA/CEAS Aeroacoustics Conference*, 2022.

[21] Quintino, N., Bonomo, L., Cordioli, J. A., Jones, M. G., Howerton, B. M., Nark, D. M., and Avallone, F., "Comparison of Impedance Eduction Test Rigs with Different Boundary-Layer Profiles," *AIAA Journal*, 2025.

[22] Rienstra, S. W., and Singh, D. K., "Nonlinear Asymptotic Impedance Model for a Helmholtz Resonator of Finite Depth," *AIAA Journal*, 2018. https://doi.org/10.2514/1.J055882.

[23] Micheli, F., Lavieille, M., and Millan, P., "ASSA, un outil de référence pour le traitement du signal en vélocimétrie laser," *Congres Francophone de Techniques Laser (CFTL)*, 2006.

[24] Minotti, A., Simon, F., and Gantié, F., "Characterization of an Acoustic Liner by Means of Laser Doppler Velocimetry in a Subsonic Flow," *Aerospace Science and Technology*, Vol. 12, No. 5, 2008, pp. 398–407. https://doi.org/10.1016/j.ast.2007.09.007.

[25] Léon, O., Piot, E., Sebbane, D., and Simon, F., "Measurement of Acoustic Velocity Components in a Turbulent Flow Using LDV and High-Repetition Rate PIV," *Experiments in Fluids*, Vol. 58, 2017, p. 72. https://doi.org/10.1007/s00348-017-2348-4.

[26] Lafont, V., Méry, F., Roncen, R., Simon, F., and Piot, E., "Liner Impedance Eduction Under Shear Grazing Flow at a High Sound Pressure Level," *AIAA Journal*, Vol. 58, No. 3, 2020, pp. 1107–1117. https://doi.org/10.2514/1.J058756.

[27] Primus, J., Piot, E., and Simon, F., "An Adjoint-Based Method for Liner Impedance Eduction: Validation and Numerical Investigation," *Journal of Sound and Vibration*, Vol. 332, No. 1, 2013, pp. 58–75. https://doi.org/10.1016/j.jsv.2012.07.051.

[28] Scarano, F., Jacob, M. C., and Gowree, E. R., "Drag reduction by means of an array of staggered circular cavities at moderate Reynolds numbers," *International Journal of Heat and Fluid Flow*, Vol. 102, 2023, p. 109142.

[29] Jaiswal, P., and Ganapathisubramani, B., "Effects of porous substrates on the structure of turbulent boundary layers," *Journal of Fluid Mechanics*, Vol. 980, 2024, p. A39. https://doi.org/10.1017/jfm.2024.45.

[30] Hoang, V. T., Jafari, A., Cazzolato, B., and Arjomandi, M., "Modification of near-wall turbulence in turbulent boundary layers due to a perforated structure," *Physics of Fluids*, July 2024. https://doi.org/https://doi.org/10.1063/5.0213907.